The Aeronautical Journal (2022), 1–18
doi:10.1017/aer.2022.68

REGULAR PAPER

Quantitative flow diagnostics of shock trains by rainbow schlieren deflectometry

T. Takeshita[1], R. Fukunaga[1], S. Nakao[1], Y. Miyazato[1,*] and K. Miki[2]

[1]The University of Kitakyushu, Department of Mechanical Systems Engineering, Kitakyushu, Japan and [2]CFD Consulting, Cleveland, OH, USA
[*]Corresponding author. Email: miyazato@kitakyu-u.ac.jp

Received: 9 September 2021; **Revised:** 30 May 2022; **Accepted:** 9 June 2022

Keywords: shock train; shock wave; rainbow schlieren deflectometry; density measurement

Abstract

A new measurement technique to reconstruct the density field of the shock-wave/boundary-layer interaction (SWBLI) in a confined duct is proposed. With this technique, it is possible to quantitatively capture in detail the structures of the density field both in the regions of the shock-systems in the central core and boundary-layer flows near the duct wall concurrently. The novel feature of the proposed technique is to make use of the schlieren images with the rainbow filters of the vertical and horizontal cutoff settings and then to reconstruct the two-dimensional density field integrated over the line-of-sight direction using the corresponding filter calibration curves. The proposed technique is applied for the first time to a shock train in a constant-area straight duct under the upstream condition of the shock train: the freestream Mach number is 1.42, the incoming boundary layer thickness normalised by the duct half height is 0.175, and the corresponding unit Reynolds number Re/m is 2.99×10^7 m^{-1}. The calculated isopycnic field depicts the streamwise and transverse density variations inside the shock train, the mixing region after the shock train, and the boundary-layer of the interaction region. This technique is shown to be capable of identifying the locations of shocks in a shock train more precisely than a conventional approach measuring the static pressure distribution along the duct wall. In addition, various quantitative visual representations such as a shadowgraphy and a bright-field schlieren can be extracted from the density field acquired by the present approach, and the spatial evolution of the shape and strength of each shock constituting the shock train as well as the boundary layer flow properties can be quantitatively clarified.

Nomenclature

A_{1e}	effective flow area just upstream of shock train (m^2)
d	ray transverse displacement (m)
f_d	focal length of decollimating lens (m)
h	duct half height (m)
h_{th}	throat half height (m)
Hue	hue (deg)
K	Gladstone-Dale constant (m^3/kg)
L	spanwise width (m)
M	Mach number
$M_{1\infty}$	freestream Mach number just upstream of shock train
n	power law index
p	wall pressure (Pa)
p_{os}	stagnation pressure in plenum chamber (Pa)
p_1	static pressure just upstream of shock train (Pa)
p_b	back pressure (Pa)
Re/m	unit Reynolds number (m^{-1})

T_b	ambient temperature (K)
u_1	streamwise velocity inside boundary layer (m/s)
$u_{1\infty}$	streamwise freestream just upstream of shock train (m/s)
x	spanwise distance (m)
y	vertical distance (m)
z	streamwise distance from test section inlet (m)
z_0	fixed streamwise location (m)
z_1	streamwise location just upstream of shock train (m)

Greek symbol

γ	specific heat ratio
δ_1	boundary layer thickness just upstream of shock train (m)
δ_1^*	displacement thickness just upstream of shock train (m)
ϵ	deflection angle of light ray (rad)
η	normal distance from duct wall (m)
θ_1	momentum thickness just upstream of shock train (m)
ρ	density (kg/m^3)
ρ_{os}	stagnation density in plenum chamber (kg/m^3)
ρ_1	density inside boundary layer just upstream of shock train (kg/m^3)
$\rho_{1\infty}$	freestream density just upstream of shock train (kg/m^3)
ρ_b	ambient density (kg/m^3)

1.0 Introduction

Over the past few decades, the development of dual-mode scramjet engines for realising next-generation propulsion systems has been consistently investigated. A dual-mode scramjet engine provides a practical solution to supersonic flight by operating over a wide range of Mach numbers. In the ramjet mode, the incoming air is compressed through a series of shock waves (i.e. precombustion shocks) in the isolater before entering the combustion chamber. This process is critical to determine overall engine performance, and thus numerous studies of the isolator shock train have been carried out in the context of design optimisation of scramjet engines [1]. In fact, such a repeated shock structure appears in a variety of flow-devices such as supersonic wind tunnels, supersonic ejectors, and supersonic inlets of aircraft engines [2]. Furthermore, these repeated shock structures have been called in many different ways in the literature including terms such as "multiple shocks", "shock system", and a series of shocks. As used herein, we refer to the shock structures in this study as a "shock train" [2]. A shock train is usually followed by a mixing region, in which the static pressure recovery takes place if the duct length is sufficient. The whole interaction region including both the shock train and the mixing region is called a "pseudo-shock". However, it is often seen that the technical terms, shock train and pseudo-shock, have been used in a confusing manner.

The previous studies [1, 2] show that a shock train occurs as a result of the interaction of a normal shock with a boundary layer developing along the wall surface in a confined duct. In almost all the previous experimental investigations, shock trains have been studied primarily by the wall pressure measurements coupled with the schlieren or shadowgraph visualisations. A primary characteristic of a shock train is determined by the pressure rise due to the shock train, the distance between the successive shocks in a shock train, the number of the shocks constituting a shock train, and the longitudinal length of a shock train. These factors are significantly influenced by three main parameters just upstream of the shock train. The first is the freestream Mach number ($M_{1\infty}$). The second is the Reynolds number based upon the boundary layer characteristic length (e.g. the boundary layer thickness, δ_1, or the boundary layer momentum thickness, θ_1). The third is the blockage ratio or the boundary layer relative thickness or the flow confinement parameter, which can be defined as the ratio δ_1/h of the boundary layer thickness δ_1 to the duct half height, h, for a two-dimensional duct or a circular duct radius [3]. In addition, it is well-known that shock waves inside a shock train oscillate across these time-mean positions and induce

https://doi.org/10.1017/aer.2022.68 Published online by Cambridge University Press

strong pressure fluctuations, leading to vibration of the fluid machines or significant noise emitting into the surrounding air [1, 2]. Recently, understanding of the behaviour of an unsteady shock train is of great need in the context of the design of scramjet engines since a higher engine thrust can be achieved when a shock train is confined inside the isolator of the scramjet engine [4–6]. Furthermore, shock train oscillations have a significant effect on the unstart problem.

The high-speed schlieren [4, 6, 7] and high-speed shadowgraphy [8] were previously used to investigate the shock train oscillations. However, the focus of those studies was on the vibration of the shock itself, and thus the unsteady flow field around shocks can not be measured at the same time. The Laser-Doppler-Velocimeter (LDV) [3, 9] and the stereo particle image velocimetry [5] are also promising approaches to investigate the internal structures of a shock train. However, the laser-based velocimetry shows that the seed particles do not seem to follow the sudden change in the velocity fields just behind the shock [10, 11]. Conventional schlieren techniques [12, 13] have been limited to use only for qualitative visualisation of the flow fields inside a shock train since it requires a cumbersome process to extract the two-dimensional density field from schlieren images. For validation purpose of the computational scheme, these experimentally measured schlieren images are often compared with the simulated ones [14–18]. Due to difficulty of obtaining the quantitative information of the flow fields inside the shock train, it is often seen that the measured wall pressure distribution is used for validation of the computational methodology [16, 18–20]. It is worth mentioning that although a good agreement between the measured and simulated wall pressure distributions or schlieren images can be achieved, the computed scalar quantities or vector fields inside the shock train could be still inaccurate. Despite of significant progress made in the experimental apparatuses, the flow measuring techniques, and the computational methods, the detailed structures inside a shock train still remain elusive.

Recently, with the development of the improved digital image processing and computational capability, several schlieren-based quantitative flow visualisations have been developed such as the background oriented schlieren (BOS) [21], the rainbow schlieren deflectometry (RSD) [22–25], and the calibrated schlieren [26]. However, most of these techniques for obtaining the density fields of shock-dominated flows have been limited to supersonic free jets. Therefore, the goal of this paper is twofold. First, a novel technique is developed for obtaining the two-dimensional density field with the shock-wave/boundary-layer interaction (SWBLI) using the rainbow schlieren deflectometry because of simple, easy to use, and relatively inexpensive in which a rainbow filter with fine colour gradations only is utilised instead of using a knife edge in a conventional schlieren system [12, 13]. Furthermore, the rainbow schlieren makes it feasible to perform a quantitative evaluation of certain refractive index fields such as shock-dominated and turbulent flows by relatively simple calculations. Second goal is to apply the proposed technique for a shock train in a confined duct. This configuration is particularly interesting since a normal shock in any fluid device with high-pressure gases tends to interact with a boundary-layer and to form a shock train in most cases. The quantitative information of the detailed structures of the flow fields inside a shock train is valuable for validating a variety of numerical simulation codes in this community. Note that there is no access to an analytical model which can quantitatively predict the quasi-periodic wavy features from successive shocks inside a shock train. In almost all previous studies, any quantitative information about the flow fields inside the shock train were not provided, and only the flow properties just downstream of a pseudo-shock were calculated for known incoming flow parameters such as the freestream Mach number, flow confinement parameter, and Reynolds number just upstream of the shock train [2]. The present study focuses on the instantaneous structure of the density field including a shock train and the following mixing region (i.e. pseudo-shock).

2.0 Experimental setup

2.1 Experimental apparatus

The experiments were performed at the intermittent blowdown compressed-air facility of the High-Speed Gasdynamics Laboratory at the University of Kitakyushu. A schematic diagram of the

https://doi.org/10.1017/aer.2022.68 Published online by Cambridge University Press

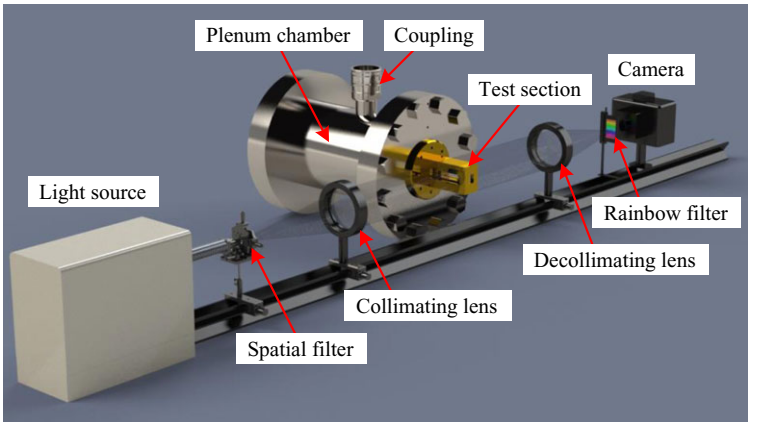

Figure 1. *Schematic drawing of experimental apparatus with rainbow schlieren optical system.*

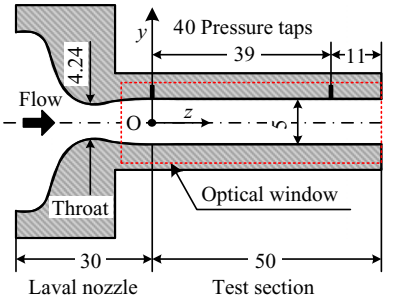

Figure 2. *Laval nozzle and test section. All dimensions are in mm.*

experimental apparatus with the rainbow schlieren system is shown in Fig. 1. Ambient air is pressured by the compressor up to 1 MPa, and then stored in the high-pressure reservoir consisting of two storage tanks with a total capacity of $2m^3$ after being filtered and dried. The supply line from the reservoir can be connected to the plenum chamber through the coupling as shown in Fig. 1. The high-pressure dry air from the reservoir is stagnated in the plenum chamber and then discharged into the atmosphere through the Laval nozzle and the test section. The plenum pressure is controlled and maintained constant during the testing with the valve.

Figure 2 shows a schematic of the Laval nozzle that is designed for Mach number = 1.5. The heights at the throat and exit are 4.24 and 5mm, respectively, and a constant spanwise width of $L = 13$mm over the full length from the nozzle inlet to exit. The shape of the Laval nozzle was generated by the method of characteristics [27] to provide uniform and parallel flow at the nozzle exit. The test section is directly connected to the exit of the Laval nozzle and consists of a constant-area straight duct with a height of $2h = 5$mm and a width of $L = 13$mm. There are 40 static pressure measuring locations with a tap of 0.5mm in diameter along the centre line of the upper wall at an equal interval of 1mm over the range from $z = 0$mm to $z = 39$mm. Each static pressure tap is connected to the digital pressure sensor (Yokogawa Model MT220) with uncertainty of 50Pa through a polyvinyl chloride tube with an inner diameter of 0.7mm and a length of 500mm. The region enclosed by the red dashed line in Fig. 2 indicates the range of an optical window for flow visualisation by the rainbow schlieren deflectometry. The operating pressure ratio of plenum pressure p_{os} to back pressure p_b (= 102.8kPa ± 0.5kPa) was held constant at 1.8 within an accuracy of ± 0.1% to produce a shock train in the test section where the room temperature T_b was 293.7K ± 0.1K.

https://doi.org/10.1017/aer.2022.68 Published online by Cambridge University Press

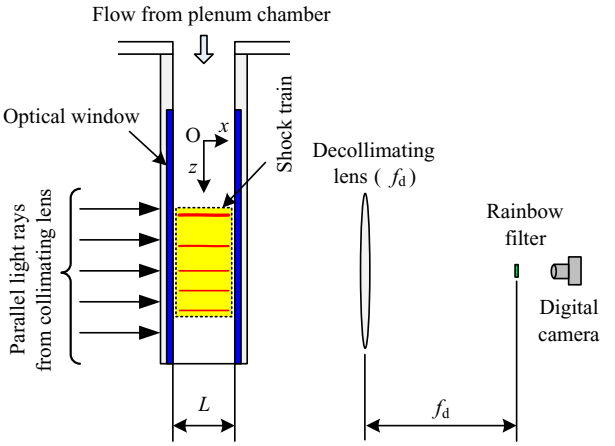

Figure 3. *Rainbow schlieren optical system.*

2.2 Rainbow schlieren optical system

As shown in Fig. 1, the rainbow schlieren system is composed of rail-mounted optical components including the continuous 250W metal halide light source (Sigmakoki IMH-250) connected to the spatial filter with a 3mm $\times$ 50μm rectangular slit through a 50μm diameter optical fiber, the collimating and decollimating lenses with 50mm diameter and 500 mm focal length, the rainbow filter, and the digital camera (Nikon D7100, effective pixels 24.1 million). Rainbow schlieren pictures were taken with an exposure time of 1/8,000s and ISO 640. Takeshita et al. [28] experimentally observed that a shock train with an incoming Mach number of 1.44 oscillates around its time-mean position with a dominant frequency of around 10Hz. Therefore, the exposure time of the present rainbow schlieren system should be short enough to freeze a shock train.

Figure 3 shows a schematic drawing of the part of the present rainbow schlieren system. In the rainbow schlieren system, when a collimated light ray is deflected through the test area, a colour image of the area revealing the ray deflections is formed on the recording medium of the digital camera. The schlieren image of the test area is then digitised to acquire a direct quantification of the light deflections using the calibration curve of the rainbow filter. The image of the rainbow filter used in the present experiments is shown in Fig. 4. In the previous preliminary experiment with the rainbow filter of 1.4mm wide [29, 30], it was found that the deflection angle of light ray after passing through the region with a strong density gradient inside a shock train exceeds the upper limit of the rainbow filter. Therefore, a new rainbow filter with a 2.5mm wide strip and continuous hue variation from $Hue = 0$ to 350 deg was fabricated in the present study.

Two sets of rainbow schlieren pictures were taken. In the first set, the rainbow filter was arranged in such a manner that the hue changes perpendicular to the z direction (called the vertical cutoff setting, herein). The vertical cutoff setting is design to render the streamwise density gradients. While for the second set, the rainbow filter was arranged in such a manner that the hue changes parallel to the z direction (called the horizontal cutoff setting, herein). The horizontal cutoff setting should render transverse density gradients. The characteristics of the rainbow filter were performed by automatically traversing the filter in intervals of 20μm $\pm$ 1μm at the schlieren cutoff plane (i.e. the location of the focal point of the decollimating lens) before starting experiments.

The calibration curves of the rainbow filter for the vertical cutoff setting and the horizontal cutoff setting are shown in Figs 5(a) and (b). The open symbols express the experimental data with precision error bars. The solid line indicates a least squares regression of the experimental data. The background hue in the rainbow filter for the present experiment corresponds to the location shown as the red arrow in each plot. The calibration of the rainbow filter in the present study was performed by traversing the

https://doi.org/10.1017/aer.2022.68 Published online by Cambridge University Press

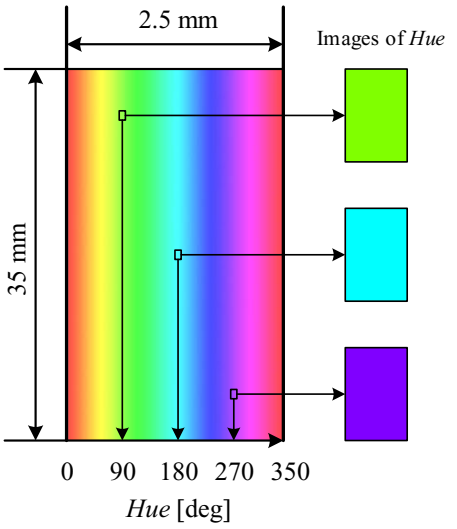

Figure 4. *Image of rainbow filter.*

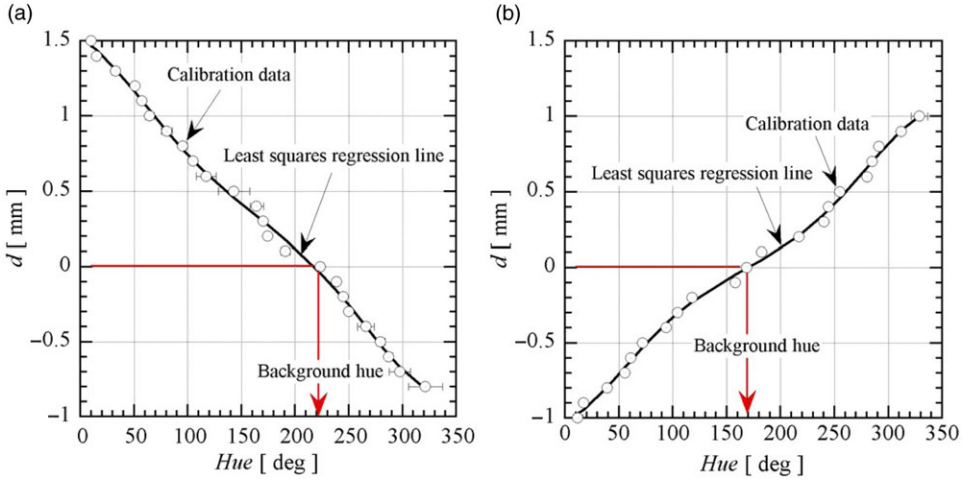

Figure 5. *Calibration curves of rainbow filters of (a) vertical and (b) horizontal cutoff settings.*

filter at the schlieren cutoff plane. Settles and Hargather [13] proposed the different type of the filter calibration by placing a calibration object with a known refractive index variation in the location of the schlieren object. Thus, it is feasible to perform a direct conversion from image pixel intensity to the corresponding refractive index gradient value. For instance, Mariani et al. [24, 25] implemented a filter calibration using a single weak focal-length lens as the calibration object. The more detailed explanation about how to design, generate, and calibrate a rainbow filter can be found elsewhere [31].

3.0 Reconstruction of density fields

Light rays coming from the decollimating lens after travelling the test section without air flows passes through a fixed location of the background hue on the rainbow filter. As shown in Fig. 3, if air flows with density gradients (e.g. shock trains) are present in the test section, some parts of the light rays

https://doi.org/10.1017/aer.2022.68 Published online by Cambridge University Press

are deflected from the original optical paths while traveling the test section. Carroll and Dutton [3] investigated the effects of the flow confinement parametre δ_1/h on the characteristic of a shock train by varying $\delta_1/h = 0.08$ to 0.49 at two freestream Mach number conditions ($M_{1\infty} = 1.6$ and 2.45). Under the condition of $M_{1\infty} = 1.6$ and $\delta_1/h = 0.40$, the surface oil flow visualisations on the duct upper as well as lower walls indicates two-dimensional flow structures in the whole flow field of the shock train except for the small corner regions beneath the foot of the first shock. Atkin and Squire [32] have studied the shock-wave/boundary-layer interaction over a range of freestream $M_{1\infty} = 1.3$ to 1.5 and found that static pressure distributions measured along the tunnel span downstream of a shock shows essentially two-dimensional flows over the middle 88 % of the tunnel width. Additionally, the flow structures in the downstream of a shock with $M_{1\infty} = 1.5$ maintains the two dimensionality across the tunnel span except for a small region near the side walls. From these observations, it is assumed that the flow properties in the spanwise direction (x direction) remain constant so that the effects of the side wall boundary layers are negligible.

The deflection angle ε of a light ray just after passing through the test section is given by the following relation based on the geometrical optics as:

$$\varepsilon(z, y) = \frac{d(z, y)}{f_d}, \tag{1}$$

where y is the vertical distance from the duct centreline, z is the streamwise distance from the test section inlet, f_d is the focal length of the decollimating lens and $d(z, y)$ is the ray transverse displacement from the location of the background hue. Here, the direction of the displacement is identical to that of the hue variation on the rainbow filter.

For a rainbow schlieren picture obtained by the vertical cutoff setting, the density gradient in the flow direction (z axis) at the duct centreline ($y = 0$) after passing through the test section with a width of L (= 13mm) is given by:

$$\frac{\partial \rho(z, 0)}{\partial z} = \frac{\varepsilon(z, 0)}{KL}, \tag{2}$$

where $K \left(= 2.26 \times 10^{-4}\ \mathrm{m^3/kg}\right)$ is the Gladstone-Dale constant. Note that the Gladstone-Dale constant has a weak dependence on the wavelength of light [31], the same value can be used. Similarly, for a rainbow schlieren picture obtained by the horizontal cutoff setting, the density gradient in the vertical direction (y axis) for a fixed $z = z_0$ is given by

$$\frac{\partial \rho\ (z_0, y)}{\partial y} = \frac{\varepsilon\ (z_0, y)}{KL}, \tag{3}$$

Integration of (2) with respect to z yields the density distribution in the z direction along the duct centreline:

$$\rho(z, 0) = \frac{1}{KL} \int_0^z \varepsilon(z, 0) dz + \rho(z_1, 0), \tag{4}$$

where $\rho(z_1, 0)$ corresponds to the density just upstream ($z = z_1$) of the shock train, and it can be estimated from the isentropic relation between the plenum pressure and the wall pressure at the location where the shock train is produced.

Integration of (3) with respect to y leads to

$$\rho\ (z_0, y) = \frac{1}{KL} \int_0^y \varepsilon\ (z_0, y)\ dy + \rho\ (z_0, 0)\ . \tag{5}$$

Given $z = z_0$, combining (4) and (5) reconstructs the one-dimensional density profile, $\rho(z_0, y)$. This process is repeated by changing the streamwise locations (z_0) in order to calculate the two-dimensional density field (i.e. $\rho(z, y)$) of the whole interaction region including the shock train.

https://doi.org/10.1017/aer.2022.68 Published online by Cambridge University Press

4.0 Flow properties just upstream of shock train

Previous studies [2, 33–35] show that the structures of a shock train are significantly affected by the undisturbed flow properties such as the freestream Mach number ($M_{1\infty}$), boundary layer properties, Reynolds number, etc. However, there is not much information available in the literature as to how to experimentally obtain these primary parameters. A brief explanation how to calculate these quantities is provided below. First, the adiabatic flow is assumed through all the flow fields including a shock train. This implies that the total temperature should remain constant throughout the whole flow field. The freestream Mach number($M_{1\infty}$) just upstream of the shock train can be determined based on the isentropic flow assumption at the outer edge of boundary layers from the plenum chamber to the location just upstream of the shock train. Assuming that there is zero pressure gradient across the boundary layers and using the measured wall pressure p_1/p_{os} normalised by the plenum pressure p_{os}, one can calculate $M_{1\infty}$ as follows:

$$M_{1\infty} = \sqrt{\frac{2}{\gamma - 1}\left[\left(\frac{p_{os}}{p_1}\right)^{\frac{\gamma-1}{\gamma}} - 1\right]}. \tag{6}$$

In order to simplify the problem, it is assumed that the effect of the boundary layer at the nozzle throat is negligible, and that the displacement thickness (δ_1^*) of the boundary layer just upstream of the shock train is the same at the upper, lower, and side walls. If A_{1e} is the effective flow area just upstream of the shock train and $2h_{th}L$ (h_{th} is the half height of the throat) is the cross-sectional area of the throat, the continuity equation between the locations of the throat and just upstream of the shock train leads to

$$A_{1e} = \frac{2h_{th}L}{M_{1\infty}}\left[\frac{(\gamma-1)M_{1\infty}^2 + 2}{\gamma + 1}\right]^{\frac{\gamma+1}{2(\gamma-1)}}. \tag{7}$$

The difference between the duct geometrical area ($2hL$) and the effective flow area (A_{1e}) is given by

$$2hL - A_{1e} = \left(L - 2\delta_1^*\right)\left(2h - 2\delta_1^*\right). \tag{8}$$

Substitution of (7) into (8) leads to

$$\frac{\delta_1^*}{h} = \frac{1 + \frac{L}{2h} - \sqrt{\left(1 + \frac{L}{2h}\right)^2 - \frac{2Lh_{th}}{M_{1\infty}h^2}\left[\frac{(\gamma-1)M_{1\infty}^2 + 2}{\gamma + 1}\right]^{\frac{\gamma+1}{2(\gamma-1)}}}}{2}. \tag{9}$$

For a boundary layer of compressible flow over a flat-plate, the ratio between the displacement thickness and the boundary layer thickness δ_1^*/δ_1 is defined by:

$$\frac{\delta_1^*}{\delta_1} \equiv \int_0^1 \left(1 - \frac{\rho_1 u_1}{\rho_{1\infty} u_{1\infty}}\right) d\left(\frac{\eta}{\delta_1}\right), \tag{10}$$

where η denotes the normal distance from the duct wall, $\rho_{1\infty}$ is the freestream density, and $u_1 = u_1(\eta)$ and $u_{1\infty}$ are the streamwise velocities inside the boundary layer and at the outer edge of the boundary layer, respectively.

The density inside the boundary layer normalised by the freestream density can be derived based on the assumptions of the constant total temperature and static pressure across the boundary layer with the equation of state for the perfect gas as follows [36]:

$$\frac{\rho_1}{\rho_{1\infty}} = \frac{1}{1 + \frac{\gamma-1}{2}M_{1\infty}^2\left[1 - \left(\frac{u_1}{u_{1\infty}}\right)^2\right]}. \tag{11}$$

https://doi.org/10.1017/aer.2022.68 Published online by Cambridge University Press

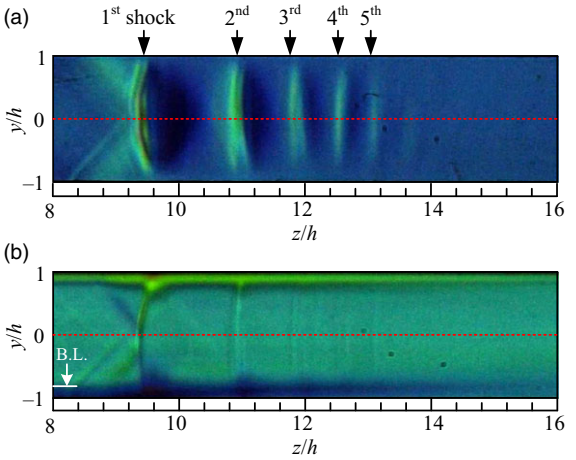

Figure 6. *Schlieren pictures with rainbow filter of (a) vertical and (b) horizontal cutoff settings. Boundary layer thickness shown in (b) is estimated from transverse density profile.*

The one-*n*th power velocity profile is assumed inside the boundary layer by

$$\frac{u_1}{u_{1\infty}} = \left(\frac{\eta}{\delta_1}\right)^{1/n}, \tag{12}$$

with $u_1 = u_{1\infty}$ for $\delta_1 \leq \eta \leq h$

Although the power law index, n, generally depends on the Reynolds number [37], a value of $n = 7$ is specified in the present study. In the case of $n = 7$, substitution of (11) and (12) into (10) leads to

$$\frac{\delta_1^*}{\delta_1} = 1 - 7(D-1)\left[\frac{D^3}{2}\ln\left(\frac{D}{D-1}\right) - \frac{D^2}{2} - \frac{D}{4} - \frac{1}{6}\right], \tag{13}$$

with $D \equiv 1 + \dfrac{2}{(\gamma-1)M_{1\infty}^2}$ [30]. Note that (10) and (11) can be also used for laminar boundary layer if the velocity profiles of the laminar boundary layers are assumed in (12).

5.0 Results and discussion

5.1 Flow visualisation

A typical rainbow schlieren picture of a shock train is presented in Fig. 6 for the case with the plenum pressure p_{os} is 185.0kPa, the back pressure p_b =102.8kPa, and the atmospheric temperature T_b is 293.7K. The flow direction is from left to right. The abscissa and ordinate denote the normalised streamwise distance from the test section inlet (the exit of the Laval nozzle) and the normalised vertical distance from the duct centreline, respectively. The red dashed line in Fig. 6 shows the duct centreline ($y/h = 0$). The freestream Mach number $M_{1\infty}$ is 1.42, the flow confinement parameter (the boundary layer relative thickness) δ_1/h is 0.175, the unit Reynolds number Re/m is 2.99×10^7 m^{-1} just upstream of the shock train. These quantities characterising a shock train were calculated using the method described in Section 4 with the measured wall pressure in Subsection 5.2.

Figure 6(a) was taken with a rainbow filter of the vertical cutoff setting to visualise the density variation in the flow direction (z direction). The overall structures of the shock train are clearly captured in this picture. The shock train consists of about five shocks as indicated in Fig. 6(a) by the down-pointing arrows. The shock train is nearly symmetrical with respect to the duct centreline. The first shock is bifurcated into a leading oblique shock and a rear oblique shock. As a result, there is a small normal part of

https://doi.org/10.1017/aer.2022.68 Published online by Cambridge University Press

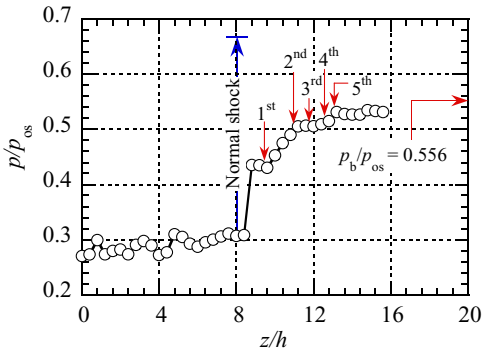

Figure 7. *Streamwise wall pressure distribution.*

the shock front near the duct centreline. The shocks following the first shock (i.e. the secondary shocks) are almost normal to the duct centreline. Figure 6(b) was taken with a rainbow filter with the horizontal cutoff setting to visualise the density variation in the vertical direction (y direction). The streamwise variation of the outer edge of the boundary layer can be clearly observed in this picture. The boundary layer thickness rapidly increases across the first shock and then decreases until it starts increasing again due to the effect of the second shock. This process repeats over the successive shocks. Consequently, there are unique feature of bumps of the boundary layer outer edge formed at each shock in the shock train.

5.2 Wall pressure distribution

The streamwise wall pressure distribution along the centreline of the duct top wall is shown with the open symbols in Fig. 7. At each measuring location, 100 data points were collected for 0.1s at the sampling rate of 1kHz and then time averaged. Similar measurements were repeated five times in order to obtain the ensemble average.

In the plots, the symbol size represents the estimated experimental uncertainty. The abscissa is the normalised streamwise distance, z/h, from the duct inlet (i.e. the exit of the Laval nozzle), and the ordinate is the ratio of the wall static pressure p to the plenum pressure p_{os}. The theoretical static pressure jump, which is calculated using the Rankin-Hugoniot relation for $M_{1\infty} = 1.42$, is shown as a reference (the blue vertical arrow). The arrow on the right vertical axis shows a value of the back pressure normalised by the plenum pressure ($p_b/p_{os} = 0.556$). In the wall pressure profile, the arrows indicate the locations of each shock in the shock train. Note that these locations were obtained from the streamwise distribution of the density gradient on the centreline of the duct as shown in Fig. 9. It is observed that these locations are consistent with the ones from the schlieren image of Fig. 6(a).

In the upstream region between the duct inlet and the first shock of the shock train, the wall pressure gradually increases due to the effect of the wall friction under the supersonic flows through a constant-area channel [38]. The wavy distribution is due to the Mach waves originated from the nozzle exit. There is a sudden increase in the wall pressure by the presence of the first shock. Note that there is no kink point at the position of the first shock as characterised by the shock-induced boundary layer separation [39]. It means that no boundary layer separation occurs at the foot of the first shock. In the wall static pressure distribution after the first shock, no distinctive changes can be observed. The theoretical pressure ratio based on the Rankine-Hugoniot relation is 0.67 for $M_{1\infty} = 1.42$ while the measured value at the location of the fifth shock of the shock train is about 0.52. The wall pressure keep raising toward the duct exit until it reaches the back pressure. The pressure recovery caused by the shock train is about 78% of the theoretical value of a single normal shock for the same incoming Mach number. The lower

https://doi.org/10.1017/aer.2022.68 Published online by Cambridge University Press

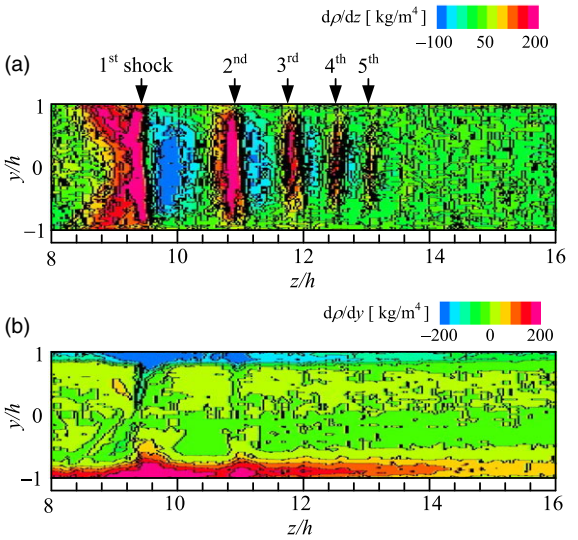

Figure 8. *Two-dimensional shock train structure represented with (a) steamwise density gradient and (b) transverse density gradient.*

pressure recovery obtained in the experiment might be attributed to the effective area reduction due to the boundary layer growth starting at the start of the interaction [40].

5.3 Density gradient fields

The schlieren pictures of a shock train taken using the vertical and horizontal cutoff settings of the rainbow filter can be utilised in order to obtain the streamwise and transverse density gradient fields. Figure 8(a) shows the streamwise density gradient field inside the shock train. With this cutoff setting, the distinct features of the five shocks are captured in detail. It is important that this method is able to clearly clarify the range and shape of compression and expansion regions across each shock in the shock train in the two-dimensional manner. As shown in Fig. 8(b), the flow features within the boundary layer associated with the interaction between shock-waves and the boundary-layer can be recognised by a large variation of the transverse density gradient field. The boundary layer exhibits a sharp rise followed by a sudden decrease beneath each shock of the shock train.

The streamwise distribution of the density gradient of the shock train along the duct centreline is illustrated in Fig. 9. A red open symbol indicates the exact location of each shock inside the shock train where the density gradient reaches the local maximum value. As seen in Fig. 9, the density gradient becomes negative in the expansion region between shocks, and the local minima in the density gradient distribution are shown as the blue open symbols. The streamwise density gradient distribution has a positive maximum value at the location of the first shock (at $z/h \sim 9.2$) and a negative minimum value behind the shock (at $z/h \sim 10$). The positive and negative peak values significantly decrease in the downstream region where the strength of shock and expansion waves become weaker toward the downstream direction. The shock train is defined as a series of genuine shocks followed by the mixing region when the duct is long enough [2]. It is important to know the exact end location of a shock train not only for the engineering and academic perspectives, but also for a better understanding of the feature of the shock train since a majority of the static pressure rise over the pseudo-shock region occurs in the shock train region [2, 41]. Although a shock train can be easily captured by optical observations such as schlieren or shadowgraph pictures, it is still difficult to quantitatively determine the end of the shock train using such conventional pictures. This is due to the fact that the region where shocks are visibly present is

https://doi.org/10.1017/aer.2022.68 Published online by Cambridge University Press

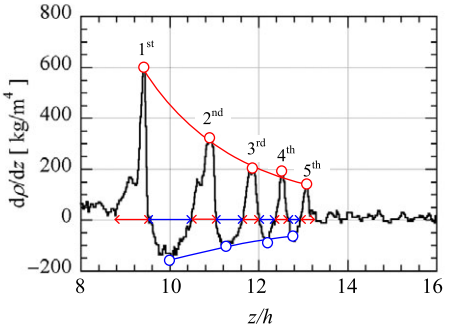

Figure 9. *Streamwise denstiy gradient profile along duct centreline.*

influenced by the contrast of the pictures, which depends strongly on the setting of a knife-edge in the schlieren system and so on.

Recently, Hunt and Gamba [5] have devised a method to find the end of a shock train from the measured wall pressure profiles. However, considering that shocks are present in the core flow away from the wall surface, it could therefore be possible that the wall pressures tend to be smeared out due to the dissipative nature of the boundary layer [1, 42]. The current methodology avoids this issues since it can directly resolve the two-dimensional feature of the shock train, and as a result, the end of the shock train can be determined with a higher accuracy (for instance, the end of the shock train is estimated $z/h = 13.2$ from Fig. 9).

5.4 Flow topology of shock train

The two-dimensional density field of the shock train can be acquired by the numerical integration of the streamwise and transverse density gradient fields of the shock train. The resulting contour plot of the density field of the shock train is depicted in Fig. 10(a). The colour map over a range from $\rho/\rho_{os} = 0.4$ to 0.7 at intervals of 0.02 is provided at the top of the figure. Here, ρ_{os} is the stagnation density in the plenum chamber. The spatial resolution of the contour is around 13μm. The downward arrows show the streamwise positions of shocks inside the shock train along the duct centreline, where a step density gradient is observed. This contour plot gives good qualitative and quantitative illustrations for the various critical features of the shock train. For instance, it is observed that the density contour is nearly symmetric about the duct centreline. There are several distinct regions such as upstream of the shock train, between successive downstream shocks, the mixing region downstream of the shock train, and the interaction zone near the wall surface. The density contour just upstream of the shock train is uniform outside the boundary layer with a thickness of $\delta_1/h = 0.175$. The density profiles begin to be affected just upstream of the leading shock of the first shock. The interval between contours gradually decreases as the shock strength get weakens toward the end of the shock train. The narrowest interval (i.e. the steepest density gradient) is seen at the position of the first shock. This is consistent with the observation of Fig. 9.

Other quantitative visual representations can be easily extracted from the density field of Fig. 10(a). For instance, Fig. 10(b) is the shadowgraphy capturing the second spatial derivative of density, which is proportional to the Laplacian of the density. This type of technique is suitable for investigating the flow fields with strong density gradients, but not the ones with mild gradients [12]. Thus, shock waves can be captured well, but not expansion waves. Another drawback of using the conventional shadowgraphy is that it provides only qualitative features unlike one as shown in Fig. 10(a). In Fig. 10(b), each shock of the shock train appears as a red line followed by a blue line. The streamwise spatial evolution of the boundary layer thickness can be clearly seen as the red regions in the vicinity of the wall. Note that the image of a shock wave taken by the conventional shadowgraph system always appears as a dark line

https://doi.org/10.1017/aer.2022.68 Published online by Cambridge University Press

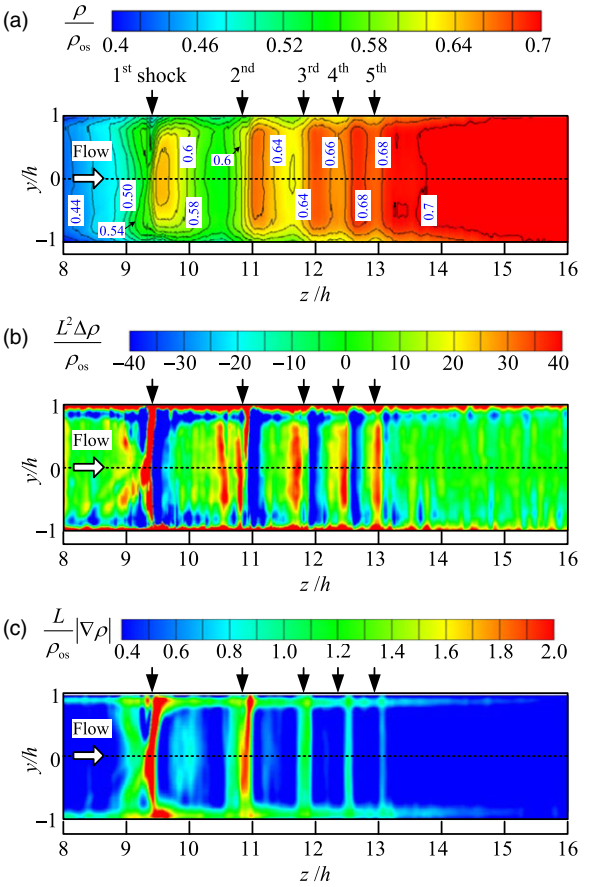

Figure 10. *Various quantitative flow visualisation for density field of shock train (a) density contour plot (b) shadowgraphy (c) bright-field schlieren.*

followed by a light line [43], which shows only the general shape of the density profile through a shock wave. The bright field schlieren shown in Fig. 10(c) or the circular cut-off schlieren [13] exhibits the magnitude of the density gradient vector, and it indicates the degree of compression and expansion in every directions. The bright-field schlieren highlights the shape and strength of the shock wave as well as the streamwise variation of the boundary layer thickness. It also quantitatively displays the degree of the strength of the expansion waves between the first and second shocks or between the second and third shocks.

The streamwise density distributions in the shock train are indicated in Fig. 11. The red line is the density profile along the duct centreline, while the blue line is the density profile inside the boundary layer ($y/h = -0.96$). In addition, the statistical error for the centreline density profile is depicted as the green solid line, where the error was obtained from ten experiments under the same pressure ratio ($p_{os}/p_b = 1.8$) and normalised by ρ_{os}. The error contains the precision error [44] only, but not the bias error since it is negligibly small when compared to the precision errors. The precision error is also affected significantly by density fluctuations caused by the unsteady behaviour of the shock train [28]. The red line shows that a successive sudden increase in the density is due to the presence of the successive shocks constituting the shock train. Although the density profiles gradually increase at both vertical locations, the variation of density fluctuations due to the presence of shocks is much larger along the centreline than the one inside the boundary layer. It should be noted that the density profile at the

https://doi.org/10.1017/aer.2022.68 Published online by Cambridge University Press

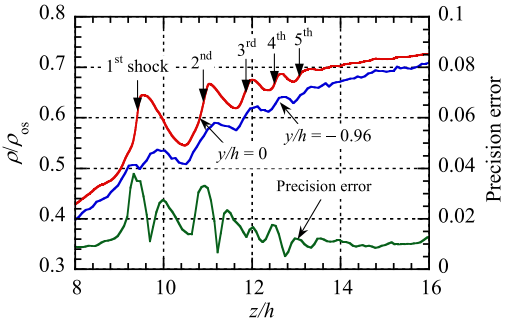

Figure 11. *Streamwise density profiles at duct centrelne and inside boundary layer.*

$y/h = -0.96$ captures the leading and rear shocks constituting the first-shock, which appears as the two broadband peaks near the first-shock. The gradual density variations are due to the weak oblique shocks. Therefore, the leading shock is not strong enough to separate the boundary layer, and the wall pressure distribution of Fig. 7 does not show a kink point near the first shock.

The precision error gradually increases till the location just upstream of the first shock and then abruptly increases and decreases across the first shock. The streamwise locations of the local maxima in the error profile coincide with the location of each shock in the shock train and of the maximum negative pressure gradient inside the expansion region between the successive shocks, respectively. In the downstream region of the shock train (after the fifth shock of the shock train), the error remains almost constant. Matuo et al. [45] experimentally investigated the oscillatory characteristics in the central region of a shock train by a static-pressure measuring system (it is called the through-tube). It was found that the distribution of the root-mean square (standard deviation) of the static pressure oscillations along the duct axis changes in a wavy form and that the peak locations agree with the time-mean positions of each shock forming the shock train. Furthermore, the maximum peak occurs at the position of the first-shock, and the following peaks gradually decrease toward the following shocks. A similar trend can be seen in the profile of the precision error shown in Fig. 11 except for the other peaks caused by the expansion waves between the successive shocks. It is challenging to capture the oscillation of the expansion waves between the successive shock by the through-tube system, since the flow fields are subject to the effect of the interaction of the shock with the unstable boundary-layer developing along the outer surface of the through-tube [8].

Transverse density profiles at three different axial locations, just ahead ($z/h = 8$) and behind ($z/h = 9.6$) the first shock and at the end ($z/h = 13.2$) of the shock train, are shown in Fig. 12. The boundary layer relative thickness on the profile of $z/h = 8$ can be determined based on the transverse density profile. The black horizontal short bar indicates the boundary layer relative thickness predicted by the method described in Section 4. The predicted value designates a location of 99 % of the freestream density. Despite the simple analytical method, it can accurately capture the boundary layer thickness. At $z/h = 9.6$ (behind the first shock), the profile shows the much thicker boundary layer, which is consistent with the observation of the schlieren pictures with rainbow filter (see Fig. 6(b)). Note that this rapid increases in the boundary layer thickness might not be due to the separation bubble underneath the first shock. In the previous study by Om and Childs [33], it was shown that both the skin-friction measurement and the alcohol technique indicate no boundary-layer separation for a shock train for the condition, $M_{1\infty} = 1.49$ and $\delta_1/h = 0.198$. In addition, Yamane et al. [35] performed the numeral simulation of a shock train in the similar condition ($M_{1\infty} = 1.7$ and $\delta_1/h = 0.4$) and observed only a small separation bubble near the first shock. When $M_{1\infty}$ is lower than around 1.8 (the upper limit of Mach number for λ- type shock train), the effect of the increased Mach number on the boundary layer is to reduce the size of the separation region, or to delay the separation [3, 16, 33, 35, 46]. Although it is hard to determine from the density profile whether or not there is a separation bubble, the separation

https://doi.org/10.1017/aer.2022.68 Published online by Cambridge University Press

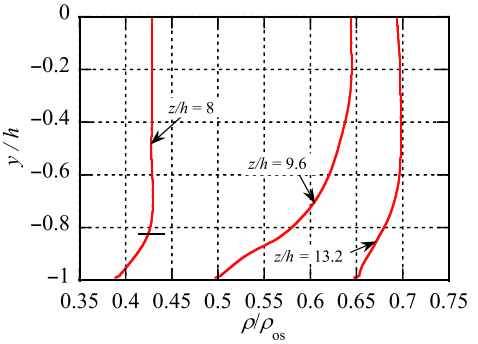

Figure 12. *Transverse density profiles at selected locations inside shock train.*

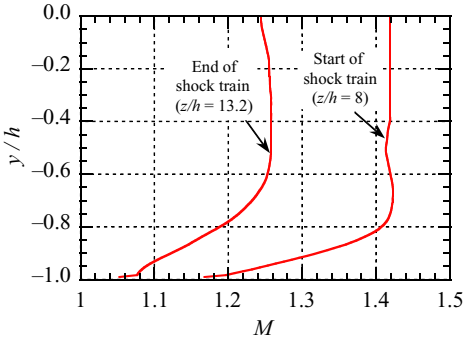

Figure 13. *Transverse Mach number profiles at start and end of shock train.*

should not happen under the present experimental condition. The transverse Mach number profiles at the two axial locations (at the start and end of the shock train), which are estimated by the density profile (Fig. 12) and the wall pressure profile (Fig. 7), are shown in Fig. 13. Note that the static pressures just ahead and behind the shock train is assumed to be constant across the duct cross-section [2]. It can be observed from Fig. 13 that the boundary layer relative thickness is around 0.4 at the end of the shock train, and that the Mach numbers are still supersonic. In addition, the freestream Mach number just upstream of the shock train is 1.42, agreeing with the value predicted from the wall static pressure within an accuracy of around 1%.

For a better understanding of the flow topology of the intricate structure of the density field inside the shock train, the bird's eye view representation of the density field is shown in Fig. 14. It can be clearly seen that weak shocks or compression waves are formed at a zone between Points a and b just upstream of the first shock. Also, it is observed that the shock surface spanning from Points c to d is a concave, which is responsible for the incoming weak shocks. From this figure, one can also quantitatively see both the lateral density variation (e.g. the red dashed line between Points e and f) from the wall surface to the freestream region, and streamwise evolution (e.g. the blue dashed line between Points g and h) of the density inside the boundary layer beneath a shock train. To the best of our knowledge, there is not much this kind of the detailed and multi-dimensional quantitative measurement data in the literature. The newly developed rainbow schlieren deflectometry system is proved to be a very effective tool capable of obtaining the fine structure of the shock train and of providing a useful validation data for numerical studies in this community.

The advantageous feature of the current rainbow schlieren technique is to perform density measurements in a microscale flows by changing the parts of the optical system such as a small source aperture,

https://doi.org/10.1017/aer.2022.68 Published online by Cambridge University Press

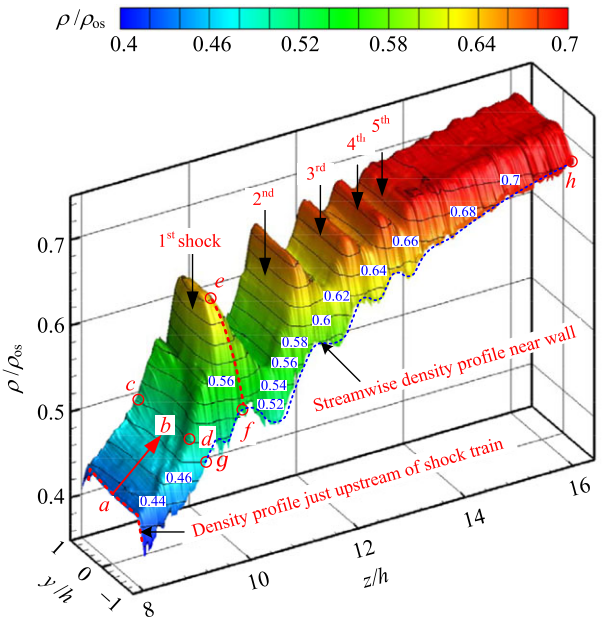

Figure 14. *Bird's eye view of density field of shock train.*

a decollimating lens with longer focal lengths, and a rainbow filter with finer colour gradations. More detailed descriptions of the rainbow schlieren technique and its applications can be found in Agrawal and Wanstall [31].

6.0 Concluding remarks

A new full two-dimensional field of view measurement technique using the rainbow schlieren deflectometry, which can quantitatively capture the density field of shock-wave/boundary-layer interaction in a confined duct, was proposed and applied for the first time to a shock train in a constant-area straight duct. The operating conditions are as follows: the freestream Mach number $M_{1\infty}$ was 1.42, the unit Reynolds number Re/m was 2.99×10^7 m^{-1} and the boundary layer relative thickness (i.e. the flow confinement parameter) δ_1/h was 0.175. The novel feature of the proposed method is to introduce the vertical and horizontal cutoff settings for the rainbow filters and to utilise the corresponding filter calibration curves simultaneously, which enable us to capture the complex features of the density gradient inside a shock train in detail.

The density field of the shock train was measured with a spatial resolution of around 13 μm. Using only wall pressure distributions, it is unfeasible to estimate the exact locations of the shocks in a shock train only. However, the shock locations, where the density gradients reach local maxima, could be precisely determined from the measured streamwise density gradient inside the shock train. It was also able to ascertain the exact end location of a shock train. With the help of the high spatial resolution, the detailed flow topology of the density field inside the shock train including the shock-boundary layer interaction was able to be quantitatively revealed. The density field acquired from the present analysis makes it possible to create other quantitative visual representations including the shadowgraphy and the bright-field schlieren, which quantitatively clarify the shape and strength of each shock constituting the shock train, the degree of the strength of the expansion waves between consecutive shocks, and the streamwise evolution of the boundary layer thickness.

https://doi.org/10.1017/aer.2022.68 Published online by Cambridge University Press

This type of detailed and quantitative measurements are desirable for the validation of numerical simulation codes and to propose a new analytical flow model that can theoretically predict the quasi-periodic wavy structure inside a shock train. The proposed technique can be easily extended for unsteady density measurements. An extension of the rainbow schlieren deflectometry for the time-dependent density field with an oscillating shock train will be a part of our future work.

Acknowledgements. The authors would like to gratefully acknowledge the assistance of graduate students Hirofumi TAKANO, Atsushi MATSUYAMA, and Takato INADOMI of the University of Kitakyushu for their invaluable support to the experimental work and exceptional skills in the fabrication of the facility.

References

[1] Gnani, F., Zare-Behtash, H. and Kontis, K. Pseudo-shock waves and their interactions in high-speed intakes, *Prog. Aerosp. Sci.*, April 2016, **82**, pp 36–56.
[2] Matsuo, K., Miyazato, Y. and Kim, H.D. Shock train and pseudo-shock phenomena in internal gas flows, *Prog. Aerosp. Sci.*, 1999, **35**(1), pp 33–100.
[3] Carroll, B.F. and Dutton, J.C. Characteristics of multiple shock wave/turbulent boundary-layer interactions in rectangular ducts, *J. Propuls. Power*, 1990, **6**(2), pp 186–193.
[4] Xiong, B., Fan, X.Q., Wang, Y. and Tao, Y. Experimental study on self-excited and forced oscillations of an oblique shock train, *J. Spacecr Rockets*, 2018, **55**(3), pp 640–647.
[5] Hunt, R.L. and Gamba, M. Shock train unsteadiness characteristics, oblique-to-normal transition, and three-dimensional leading shock structure, *AIAA J*, 2018, **56**(4), pp 1569–1587.
[6] Hou, W., Chang, J., Xie, Z., Wang, Y., Wu, L. and Bao, W. Behavior and flow mechanism of shock train self-excited oscillation influenced by background waves, *Acta Astronaut.*, January 2020, **166**, pp 29–40.
[7] Gawehn, T., Gülhan, A., Al-Hasan, N.S. and Schnerr, G.H. Experimental and numerical analysis of the structure of pseudo-shock systems in Laval nozzles with parallel side walls, *Shock Waves*, 2010, **20**(4), pp 297–306.
[8] Grzona, A. and Olivier, H. Shock train generated turbulence inside a nozzle with a small opening angle, *Exp. Fluids*, 2011, **51**(3), pp 621–639.
[9] Sugiyama, H., Arai, T., Abe, H., Takahashi, T. and Takayama, K. Flow mechanism of λ-type pseudoshock eaves in a straight-square duct, *Trans. Jpn. Soc. Mech. Eng., Ser. B*, 1990, 56(552), pp 330–335.
[10] Koike, S., Suzuki, K., Kitamura, E., Hirota, M., Takita, K., Masuya, G.O. and Matsumoto, M. Measurement of vortices and shock waves produced by ramp and twin jets, *J. Propuls. Power*, 2006, **22**(5), pp 1059–1067.
[11] Wernet, M.P. Application of Tomo-PIV in a large-scale supersonic jet flow facility, *Exp. Fluids*, 2016, **57**(9), 144.
[12] Settles, G.S. Schlieren and Shadowgraph Techniques, Springer, 2001.
[13] Settles, G.S. and Hargather, M.J. A review of recent developments in schlieren and shadowgraph techniques, *Meas. Sci. Technol.*, 2017, **28**(4), 042001.
[14] Sun, L.Q., Sugiyama, H., Mizobata, K. and Fukuda, K. Numerical and experimental investigations on the Mach 2 pseudo-shock wave in a square duct, *J. Vis.*, 2003, **6**(4), pp 363–370.
[15] Sun, L., Sugiyama, H., Mizobata, K., Minato, R. and Tojo, A. Numerical and experimental investigations on Mach 2 and 4 pseudo-shock waves in a square duct, *Trans. Jpn. Soc. Aeronaut. Space Sci.*, 2004, **47**(156), pp 124–130.
[16] Morgan, B., Duraisamy, K. and Lele, S.K. Large-eddy simulations of a normal shock train in a constant-area isolator, *AIAA J.*, 2014, **52**(3), pp 539–558.
[17] Cai, J., Zhou, J., Liu, S. and Lin, Z. Effects of dynamic backpressure on shock train motions in straight isolator, *Acta Astronaut.*, December 2017, **141**, pp 237–247.
[18] Gnani, F., Zare-Behtash, H., White, C. and Kontis, K. Numerical investigation on three-dimensional shock train structures in rectangular isolators, *Eur. J. Mech. B Fluids*, 2018, **72**, pp 586–593.
[19] Fiévet, R., Koo, H., Raman, V. and Auslender, A.H. Numerical investigation of shock-train response to inflow boundary-layer variations, *AIAA J*, 2017, **55**(9), pp 2888–2901.
[20] Gnani, F., Zare-Behtash, H., White, C. and Kontis, K. Effect of back-pressure forcing on shock train structures in rectangular channels, *Acta Astronaut.*, April 2018, **145**, pp 471–481.
[21] Nicolas, F., Donjat, D., Léon, O., Le Besnerais, G., Champagnat, F. and Micheli, F. 3D reconstruction of a compressible flow by synchronized multi-camera BOS, *Exp Fluids*, 2017, **58**(5), 46.
[22] Takano, H., Kamikihara, D., Ono, D., Nakao, S., Yamamoto, H. and Miyazato, Y. Three-dimensional rainbow schlieren measurements in underexpanded sonic jets from axisymmetric convergent nozzles, *J. Thermal Sci.*, 2016, **25**(1), pp 78–83.
[23] Maeda, H., Fukuda, H., Kubo, K., Nakao, S., Ono, D. and Miyazato, Y. Structure of underexpanded supersonic jets from axisymmetric Laval nozzles, *J. Flow Vis. Image Process.*, 2018, **25**(1), pp 33–46.
[24] Mariani, R., Zang, B., Lim, H.D., Vevek, U.S., New, T.H. and Cui, Y.D. A comparative study on the use of Calibrated and Rainbow Schlieren techniques in axisymmetric supersonic jets, *Flow Meas. Instrum.*, April 2019, **66**, pp 218–228.
[25] Mariani, R., Lim, H.D., Zang, B., Vevek, U.S., New, T.H. and Cui, Y.D. On the application of non-standard rainbow schlieren technique upon supersonic jets, *J. Vis.*, 2020, **23**(3), pp 383–393.

https://doi.org/10.1017/aer.2022.68 Published online by Cambridge University Press

[26] Nazari, A.Z., Ishino, Y., Ishiko, Y., Ito, F., Kondo, H., Yamada, R., Motohiro, T., Miyazato, Y. and Nakao, S. Multi-schlieren CT measurements of supersonic microjets from circular and square micro nozzles, *J. Flow Control, Meas. Vis.*, 2020, **8**(3), pp 77–101.
[27] Crown, J.C. Design of nozzles having continuous wall curvature, *J. Aeronaut. Sci.*, 1952, **19**(5), pp 358–359.
[28] Takeshita, T., Nakao, S. and Miyazato, Y. Application of Mach-Zehnder interferometers for isolator shock trains, *ACC J.*, 2019, **25**(1), pp 68–77.
[29] Takeshita, T., Takano, H., Ono, D., Nakao, S. and Miyazato, Y. Rainbow schlieren visualization of shock trains in rectangular ducts, *23rd Conference of the International Scociety for Air Breathing Engines*, 2017, 21452.
[30] Matsuyama, A., Nakao, S., Ono, D., Miyazato, Y. and Kashitani, M. Two-dimensional quantitative visualization of isolator shock trains by rainbow schlieren deflectometry, *EPJ Web of Conferences*, 2018, **180**, 02063.
[31] Agrawal, A.K. and Wanstall, C.T. Rainbow schlieren deflectometry for scalar measurements in fluid flows, *J. Flow Vis. Image Process.*, 2018, **25**(3–4), pp 329–357
[32] Atkin, C.J. and Squire, L.C. A study of the interaction of a normal shock wave with a turbulent boundary layer at Mach numbers between 1.30 and 1.55, *Eur. J. Mech. B Fluids*, 1992, **11**(1), pp 93–118.
[33] Om, D. and Childs, M.E. Multiple transonic shock-wave/turbulent boundary-layer interaction in a circular duct, *AIAA J.*, 1985, **23**(10), pp 1506–1511.
[34] Carroll, B.F. and Dutton, J.C. Turbulence phenomena in a multiple normal shock wave/turbulent boundary-layer interaction, *AIAA J.*, 1992, **30**(1), pp 43–48.
[35] Yamane, R., Oshima, S., Nakamura, Y., Ishii, T. and Park, M.K. Numerical simulation of pseudoshock in straight channels, *JSME Int. J. Ser. B: Fluids Ther. Eng.*, 1995, **38**(4), pp 549–554.
[36] Tuchker, M. Approximate calculation of turbulent boundary-layer development in compressible flow, *NACA*, 1951, Technical Note No. 2337.
[37] Gerhart, P.M., Gross, R.J. and Hochstein, J.I. *Fundamentals of Fluid Mechanics*, 2nd ed., Addison-Wesley Publishing Com., 1993, p 487.
[38] Shapiro, A.H. *The Dynamics and Thermodynamics of Compressible Flid Flow*, Vol. **2**. Ronald Press, New York, 1953, pp 159–178.
[39] Seddon, J. The flow produced by interaction of a turbulent boundary layer with a normal shock wave of strength sufficient to cause separation, *Aero. Res. Counc., R&M 3502*, 1960, pp 159–178.
[40] Matsuo, K., Miyazato, Y. and Kim, H.D. Mass-averaging pseudo-shock model in a straight flow passage, *Proc. Inst. Mech. Eng. G J Aeros. Eng.*, 1999, **213**(6), pp 365–375.
[41] Sullins, G. and McLafferty, G. Experimental results of shock trains in rectangular ducts, 1992, AlAA Paper 92-5103.
[42] Weiss, A., Grzona, A. and Olivier, H. Behavior of shock trains in a diverging duct, *Exp. Fluids*, 2010, **49**(2), pp 355–365.
[43] Liepmann, H.W. and Roshko, A. *Elements of Gasdynamics*. Dover Publishing, INC., Mineola, New York, 2001, pp 162–163.
[44] Coleman, H.W. and Steele, W.G. Experimentation, Validation, and Uncertainty Analysis for Engineers, 3rd ed. *John Wiley & Sons*, 2009.
[45] Matsuo, K., Mochizuki, H., Miyazato, Y. and Gohya, M. Oscillatory characteristics of a pseudo-shock wave in a rectangular straight duct, *JSME Int. J. Ser. B: Fluids Ther. Eng.*, 1993, **36**(2), pp 222–229.
[46] Carroll, B.F., Lopez-Fernandez, P.A. and Dutton, J.C. Computations and experiments for a multiple normal shock/boundary-layer interaction, *J. Propuls. Power*, 1993, **9**(3), pp 405–411.

Cite this article: Takeshita T., Fukunaga R., Nakao S., Miyazato Y. and Miki K. Quantitative flow diagnostics of shock trains by rainbow schlieren deflectometry. *The Aeronautical Journal*, https://doi.org/10.1017/aer.2022.68